

Dynamical Relativistic Effects in Breakup Processes of Halo Nuclei

Kazuyuki OGATA¹ and Carlos A. BERTULANI²

¹*Department of Physics, Kyushu University, Fukuoka 812-8581, Japan*

²*Department of Physics, Texas A&M University, Commerce, TX 75429, USA*

The continuum-discretized coupled-channels (CDCC) method is used to study the breakup of weakly-bound nuclei at intermediate energies collisions. For large impact parameters, the Eikonal CDCC (E-CDCC) method was applied. The effects of Lorentz contraction on the nuclear and Coulomb potentials have been investigated in details. Such effects tend to increase cross sections appreciably. We also show that, for loosely-bound nuclei, the contribution of the so-called close field is small and can be neglected.

§1. Introduction

The properties of unstable nuclei are one of the most important subjects in science. The breakup reactions of such short-lived nuclei provide us with plentiful information on their static and dynamical features. Among them, the responses of unstable nuclei to electromagnetic fields have been intensively studied. For this purpose, usually a heavy (highly charged) target such as ²⁰⁸Pb is adopted and many of the breakup experiments have been performed at intermediate energies, say, 100–250 MeV per nucleon, to minimize possible “contaminations” due to nuclear breakup and higher-order breakup processes.

It is well known that a theoretical description of breakup reactions at intermediate energies requires a relativistic treatment of the reaction dynamics, though only a relativistic modification on the kinematics has been usually included. The virtual photon theory, or, equivalent photon method, is a fully relativistic reaction model to describe the excitation of a projectile under electromagnetic fields caused by a target nucleus. However, it cannot deal with the nuclear breakup and higher-order breakup processes. To extract reliable physics quantities such as B(E1)-values and asymptotic normalization coefficients from breakup experiments, evaluation of the contributions from the above mentioned processes is necessary.

In our recent Letter,¹⁾ we developed a full coupled-channel calculation including a relativistic treatment of not only the kinematics but also the dynamics, based on the Continuum-Discretized Coupled-Channels method (CDCC)²⁾ with the eikonal approximation, i.e., eikonal CDCC (E-CDCC).^{3),4)} An essential ingredient of the relativistic CC calculation was the proper treatment of nuclear and Coulomb coupling potentials between the projectile and the target. We adopted the form of the Coulomb dipole and quadrupole interactions shown in Ref. 5), which was obtained from a relativistic Liénard-Wiechert potential with so-called far-field approximation. As for the nuclear potential, the conjecture of Feshbach and Zabeck⁶⁾ was adopted. We showed that the dynamical relativistic corrections are responsible for an increase of about 15% in the breakup cross sections of ⁸B and ¹¹Be projectiles by ²⁰⁸Pb at 250 MeV/nucleon. Another important finding was that the nuclear breakup and

higher-order breakup processes were significant even at 250 MeV/nucleon.

In the present paper, we show a more detailed analysis of the dynamical relativistic effects on the breakup cross sections of ^8B and ^{11}Be projectiles by ^{208}Pb at 250 MeV/nucleon. First, we investigate the relativistic effects on the double differential breakup cross section, which clarifies how relativity affects the cross section at several emission angles θ and breakup energies ϵ . Differences in the relativistic effects between ^8B and ^{11}Be breakup are also discussed. Second, the contribution of the nuclear breakup and higher-order processes are shown on the ϵ - θ plane. Third, a quantum mechanical correction in the breakup amplitude obtained by E-CDCC is carried out, which enables one to perform fully relativistic and quantum mechanical CC calculations of breakup reactions at intermediate energies. Fourth, the contribution from so-called close-fields, which are neglected in obtaining the relativistic Coulomb interactions,⁵⁾ is evaluated by means of the first-order time-dependent theory.

The paper is constructed as follows. In §2, we summarize some formulae of E-CDCC and show how to include the dynamical relativistic corrections to the coupling potentials. The contribution from the close-fields to the breakup process is also formulated. In §3, we present our numerical results and discuss the relevant physics. Finally, we give a summary in §4.

§2. Formulation

2.1. Relativistic CDCC

We start with the following nonrelativistic E-CDCC equations^{3),4)} for a three-body reaction between a projectile P, consisting of a core (C) and a valence nucleon v, and a target nucleus T:

$$\frac{i\hbar^2}{E_c} K_c^{(b)}(z) \frac{d}{dz} \psi_c^{(b)}(z) = \sum_{c'} \mathfrak{F}_{cc'}^{(b)}(z) \mathcal{R}_{cc'}^{(b)}(z) \psi_{c'}^{(b)}(z) e^{i(K_{c'} - K_c)z}, \quad (2.1)$$

where c denotes the channel indices $\{i, \ell, m\}$; $i > 0$ ($i = 0$) stands for the i th discretized-continuum (ground) state, and ℓ and m are, respectively, the orbital angular momentum between the constituents (C and v) of P and its projection on the z -axis taken to be parallel to the incident beam. We neglect the internal spins of C and v for simplicity. b is the impact parameter (or transverse coordinate) in the collision of P and T, which is defined by $b = \sqrt{x^2 + y^2}$ with $\mathbf{R} = (x, y, z)$, the relative coordinate of P from T in the Cartesian representation. Note that in Eq. (2.1) b is relegated to a superscript since it is not a dynamical variable. The total energy and the asymptotic wave number of P are denoted by E_c and K_c , respectively, and $\mathcal{R}_{cc'}^{(b)}(z) = (K_{c'}R - K_{c'}z)^{i\eta_{c'}} / (K_cR - K_cz)^{i\eta_c}$ with η_c the Sommerfeld parameter. The local wave number $K_c^{(b)}(z)$ of P is defined by energy conservation as

$$E_c = \sqrt{(m_P c^2)^2 + [\hbar c K_c^{(b)}(z)]^2} + \frac{Z_P Z_T e^2}{R}, \quad (2.2)$$

where m_P is the mass of P and Z_{Pe} (Z_{Te}) is the charge of P (T). The reduced coupling potential $\mathfrak{F}_{cc'}^{(b)}(z)$ is given by

$$\mathfrak{F}_{cc'}^{(b)}(z) = \mathcal{F}_{cc'}^{(b)}(z) - \frac{Z_P Z_T e^2}{R} \delta_{cc'}, \quad (2.3)$$

where

$$\mathcal{F}_{cc'}^{(b)}(z) = \langle \Phi_c | U_{CT} + U_{vT} | \Phi_{c'} \rangle_{\xi} = \mathcal{F}_{cc'}^{\text{nucl}(b)}(z) + \mathcal{F}_{cc'}^{\text{Coul}(b)}(z), \quad (2.4)$$

$$\mathcal{F}_{cc'}^{\text{nucl}(b)}(z) = \left\langle \Phi_c | U_{CT}^{\text{nucl}} + U_{vT}^{\text{nucl}} | \Phi_{c'} \right\rangle_{\xi}, \quad (2.5)$$

$$\mathcal{F}_{cc'}^{\text{Coul}(b)}(z) = \left\langle \Phi_c | U_{CT}^{\text{Coul}} + U_{vT}^{\text{Coul}} | \Phi_{c'} \right\rangle_{\xi}. \quad (2.6)$$

$\Phi_c(\xi)$ denotes the internal wave functions of P, with ξ the coordinate of v relative to C, and U_{CT} (U_{vT}) is the potential between C (v) and T consisting of nuclear and Coulomb parts. Furthermore, in actual calculations, we use the multipole expansion for each term on the right-hand-side of Eq. (2.4):

$$\mathcal{F}_{cc'}^{\text{nucl}(b)}(z) = \sum_{\lambda} \mathcal{F}_{cc',\lambda}^{\text{nucl}(b)}(z), \quad (2.7)$$

$$\mathcal{F}_{cc'}^{\text{Coul}(b)}(z) = \sum_{\lambda} \mathcal{F}_{cc',\lambda}^{\text{Coul}(b)}(z). \quad (2.8)$$

The explicit form of the multipoles is given in Ref. 4).

In Ref. 5), the relativistic form of the electric dipole (E1) and quadrupole (E2) interactions are given by

$$V_{E1\mu}^{\text{rel}}(b, z, \hat{\xi}) = \sqrt{\frac{2\pi}{3}} \xi Y_{1\mu}(\hat{\xi}) \frac{\gamma Z_T e e_{E1}}{(b^2 + \gamma^2 z^2)^{3/2}} \begin{cases} \mp b, & (\text{if } \mu = \pm 1) \\ \sqrt{2}z & (\text{if } \mu = 0) \end{cases}, \quad (2.9)$$

$$V_{E2\mu}^{\text{rel}}(b, z, \hat{\xi}) = \sqrt{\frac{3\pi}{10}} \xi^2 Y_{2\mu}(\hat{\xi}) \frac{\gamma Z_T e e_{E2}}{(b^2 + \gamma^2 z^2)^{5/2}} \times \begin{cases} b^2, & (\text{if } \mu = \pm 2) \\ \mp(\gamma^2 + 1)bz, & (\text{if } \mu = \pm 1) \\ \sqrt{2/3}(2\gamma^2 z^2 - b^2) & (\text{if } \mu = 0) \end{cases}, \quad (2.10)$$

where $e_{E\lambda} = [Z_v(A_C/A_P)^\lambda + Z_C(-A_v/A_P)^\lambda]e$ are effective charges for $\lambda = 1$ and 2 multipolarities for the breakup of $P \rightarrow C + v$; A_j ($j = C, v, P$) represents the mass number of the particle j . The Lorentz contraction factor is denoted by $\gamma = (1 - v^2/c^2)^{-1/2}$, where v is the velocity of P. Equations (2.9) and (2.10) are obtained with so-called far-field approximation,⁷⁾ i.e., R is assumed to be always larger than both $\xi A_v/A_P$ and $\xi A_C/A_P$. Derivation of these equations is described in detail in Ref. 8). In addition, for magnetic dipole excitations (not considered here),

$$V_{M1\mu}^{\text{rel}}(b, z, \hat{\xi}) = i \sqrt{\frac{2\pi}{3}} \bar{M}_{1\mu}(\hat{\xi}) \frac{v}{c} \frac{\gamma Z_T e}{(b^2 + \gamma^2 z^2)^{3/2}} \begin{cases} \pm b, & (\text{if } \mu = \pm 1) \\ 0 & (\text{if } \mu = 0) \end{cases}, \quad (2.11)$$

where $\bar{M}_{1\mu}(\boldsymbol{\xi})$ is the intrinsic M1 operator.

One may find easily that $V_{E1\mu}^{\text{rel}}$ and $V_{E2\mu}^{\text{rel}}$ are, respectively, obtained from their nonrelativistic expressions $V_{E1\mu}$ and $V_{E2\mu}$ as

$$\begin{aligned} V_{E1\pm 1}^{\text{rel}}(b, z, \hat{\boldsymbol{\xi}}) &= \gamma V_{E1\pm 1}(b, \gamma z, \hat{\boldsymbol{\xi}}), & V_{E10}^{\text{rel}}(b, z, \hat{\boldsymbol{\xi}}) &= V_{E10}(b, \gamma z, \hat{\boldsymbol{\xi}}), \\ V_{E2\pm 2}^{\text{rel}}(b, z, \hat{\boldsymbol{\xi}}) &= \gamma V_{E2\pm 2}(b, \gamma z, \hat{\boldsymbol{\xi}}), & V_{E2\pm 1}^{\text{rel}}(b, z, \hat{\boldsymbol{\xi}}) &= \frac{\gamma^2 + 1}{2} V_{E2\pm 1}(b, \gamma z, \hat{\boldsymbol{\xi}}), \\ V_{E20}^{\text{rel}}(b, z, \hat{\boldsymbol{\xi}}) &= \gamma V_{E20}(b, \gamma z, \hat{\boldsymbol{\xi}}). \end{aligned}$$

Thus, we can include the dynamical relativistic corrections in E-CDCC by carrying out the replacement

$$\mathcal{F}_{cc',\lambda}^{\text{Coul}(b)}(z) \rightarrow \gamma f_{\lambda,m-m'} \mathcal{F}_{cc',\lambda}^{\text{Coul}(b)}(\gamma z) \quad (2.12)$$

with

$$f_{\lambda,\mu} = \begin{cases} 1/\gamma, & (\lambda = 1, \mu = 0) \\ (\gamma^2 + 1)/(2\gamma), & (\lambda = 2, \mu = \pm 1) \\ 1 & (\text{otherwise}) \end{cases} . \quad (2.13)$$

Correspondingly, we use

$$\frac{Z_P Z_T e^2}{R} \delta_{cc'} \rightarrow \gamma \frac{Z_P Z_T e^2}{\sqrt{b^2 + (\gamma z)^2}} \delta_{cc'} \quad (2.14)$$

in Eqs. (2.2) and (2.3). For the nuclear coupling potential $\mathcal{F}_{cc',\lambda}^{\text{nucl}(b)}(z)$, we adopt

$$\mathcal{F}_{cc',\lambda}^{\text{nucl}(b)}(z) \rightarrow \gamma \mathcal{F}_{cc',\lambda}^{\text{nucl}(b)}(\gamma z) \quad (2.15)$$

following the conjecture of Feshbach and Zabek.⁶⁾ In the present CC calculation, the Lorentz contraction factor γ may have channel dependence, i.e., $\gamma = E_c/(m_P c^2)$, which we approximate using the value in the incident channel, i.e., $E_0/(m_P c^2)$. This can be justified since the energy transfer to the projectile is significantly small compared with the incident energy, in the reactions considered here.

Solving Eq. (2.1) under the boundary condition

$$\lim_{z \rightarrow -\infty} \psi_c^{(b)}(z) = \delta_{c0}, \quad (2.16)$$

where 0 denotes the incident channel, one obtains the following form of the eikonal scattering amplitude:

$$f_{c0}^E = f_{c0}^{\text{Ruth}} \delta_{c0} + \frac{2\pi}{iK_0} \sum_L f_{L;c0}^{\prime E} Y_{Lm-m_0}(\hat{\mathbf{K}}'_c), \quad (2.17)$$

where f_{c0}^{Ruth} is the Rutherford amplitude. The partial scattering amplitude $f_{L;c0}^{\prime E}$ is defined by

$$f_{L;c0}^{\prime E} = \frac{K_0}{K_c} \mathcal{H}_c^{(b;c;L)} \sqrt{\frac{2L+1}{4\pi}} i^{(m-m_0)} [\mathcal{S}_{c0,L} - \delta_{c0}], \quad (2.18)$$

where

$$\mathcal{S}_{c0,L} \equiv \lim_{z \rightarrow \infty} \psi_c^{(b_{c;L})}(z) \quad (2.19)$$

with $b_{c;L} = (L + 1/2)/K_c$, and $\mathcal{H}_{c,L} \equiv \exp[2i\eta_c \ln(L + 1/2)]$.

The quantum mechanical (QM) correction in the scattering amplitude can be performed if one replaces $f_{L;c0}^E$ for small L , say, $L < L_C$, by the QM partial amplitude obtained with the conventional QM CDCC:

$$\begin{aligned} f_{L;c0}^Q \equiv & \sum_{J=|L-\ell|}^{L+\ell} \sum_{L_0=|J-\ell_0|}^{J+\ell_0} \sqrt{\frac{2L_0+1}{4\pi}} (\ell_0 m_0 L_0 0 | J m_0) (\ell m L m_0 - m | J m_0) \\ & \times (S_{iL\ell, i_0 L_0 \ell_0}^J - \delta_{i_0} \delta_{L L_0} \delta_{\ell \ell_0}) e^{i(\sigma_L + \sigma_{L_0})} (-)^{m-m_0}, \end{aligned} \quad (2.20)$$

where σ_L is the Coulomb phase shift and J is the total angular momentum of the three-body system. This correction is valid if $f_{L;c0}^E = f_{L;c0}^Q$ for $L \geq L_C$; this is in fact the definition of L_C . Note that in a full QM calculation, i.e., without the eikonal approximation, inclusion of the dynamical relativistic corrections in the coupling potentials is very complicated and actually inconsistent with the formalism. Fortunately, however, it was shown in our previous Letter¹⁾ that the dynamical relativistic corrections are necessary only for large L , where the scattering processes are well described by the eikonal approximation. Thus, using the following scattering amplitude

$$f_{c0} = f_{c0}^{\text{Ruth}} \delta_{c0} + \frac{2\pi}{iK_0} \sum_{L < L_C} f_{L;c0}^Q Y_{L m - m_0}(\hat{\mathbf{K}}'_c) + \frac{2\pi}{iK_0} \sum_{L \geq L_C} f_{L;c0}^E Y_{L m - m_0}(\hat{\mathbf{K}}'_c), \quad (2.21)$$

with the dynamical relativistic correction in the evaluation of $f_{L;c0}^E$, one can carry out a relativistic QM calculation including both nuclear and Coulomb couplings, and also all higher-order processes, i.e., a *relativistic CDCC* calculation.

2.2. Contribution from close-fields to Coulomb breakup processes

As mentioned in §2.1, we have used the relation between the relativistic and nonrelativistic $E\lambda$ ($\lambda = 1$ or 2) interactions that is appropriate for the far-field collisions. To verify this assumption, we evaluate the contribution from the $E1$ close-field collisions in the following, on the basis of the first-order time-dependent theory.

We start with the multipole-expansion form of the Liénard-Wiechert potential for close-field collisions given by Eq. (9b) of Ref. 7):

$$\phi^{\text{close}}(\mathbf{r}, \mathbf{R}) = \sum_{\lambda\mu\mu'} 4\pi Y_{\lambda\mu}^*(\hat{\mathbf{r}}) \sum_{\Lambda=0,2,4,\dots} i^\Lambda R_{\lambda,\lambda-\Lambda}(r, R) A_{\lambda\mu,\lambda-\Lambda\mu'}(\beta) Y_{\lambda-\Lambda,\mu'}(\hat{\mathbf{R}}), \quad (2.22)$$

where \mathbf{r} is the coordinate of a point charge in P relative to the center of mass (c.m.) of P, and \mathbf{R} is the relative coordinate between the c.m. of P and another point charge in T. In Eq. (2.22), $R_{\lambda,\lambda'}$ and $A_{\lambda\mu,\lambda'\mu'}$ are given by

$$R_{\lambda,\lambda'}(r, R) = \frac{1}{\sqrt{rR}} \int_0^\infty \frac{dq}{q} J_{\lambda+1/2}(qr) J_{\lambda'+1/2}(qR), \quad (2.23)$$

$$A_{\lambda\mu,\lambda'\mu'}(\beta) = \sum_{X \text{ even}} g_X(\beta) \langle Y_{\lambda'\mu'}(\hat{\mathbf{q}}) | P_X(\theta_q) | Y_{\lambda\mu}(\hat{\mathbf{q}}) \rangle, \quad (2.24)$$

where

$$g_X(\beta) = \frac{(2X+1)}{\beta} Q_X(\beta^{-1}), \quad Q_X(z) = \frac{1}{2} \int_{-1}^1 dt \frac{P_X(t)}{z-t} \quad (2.25)$$

with $\beta = v/c$ and \mathbf{q} is the momentum conjugate to the relative coordinate $\mathbf{r} - \mathbf{R}$.

If we consider E1 transitions, i.e., $\lambda = 1$, we see that $L = 0$ is only allowed, since L must be even and $\lambda - L$ is not negative. We then have

$$\phi_{(\lambda=1)}^{\text{close}}(\mathbf{r}, \mathbf{R}) = \sum_{\mu\mu'} 4\pi Y_{1\mu}^*(\hat{\mathbf{r}}) R_{1,1}(r, R) A_{1\mu,1\mu'}(\beta) Y_{1\mu'}(\hat{\mathbf{R}}) \quad (2.26)$$

with

$$A_{1\mu,1\mu'}(\beta) = \left\{ g_0(\beta) - \sqrt{\frac{2}{5}} (1\mu 20 | 1\mu) g_2(\beta) \right\} \delta_{\mu\mu'}. \quad (2.27)$$

The diagonal radial part $R_{\lambda,\lambda}(r, R)$ is given by Eq. (6) of Ref. 7) and we have

$$R_{1,1}(r, R) = \frac{1}{3} \frac{R}{r^2}. \quad (2.28)$$

Note that we assume here $r > R$. From Eqs. (4b) and (4c) of Ref. 7), one can obtain explicit form of $g_0(\beta)$ and $g_2(\beta)$:

$$g_0(\beta) = \frac{1}{\beta} \frac{1}{2\beta} \ln \left(\frac{1+\beta}{1-\beta} \right), \quad (2.29)$$

$$g_2(\beta) = \frac{5}{4\beta} \left(\frac{3}{\beta^2} - 1 \right) \ln \left(\frac{1+\beta}{1-\beta} \right) - \frac{15}{2\beta^2}. \quad (2.30)$$

Thus, the relativistic Coulomb dipole interaction between T and a proton inside P for close-field collisions is given by

$$\bar{V}_{1\mu}^{\text{close}}(\mathbf{r}, \mathbf{R}) = \sqrt{\frac{2\pi}{3}} Z_T e^2 \frac{1}{r^2} Y_{1\mu}^*(\hat{\mathbf{r}}) \{g_0(\beta) + c_\mu g_2(\beta)\} \begin{cases} \sqrt{2}z & \text{if } \mu = 0 \\ \mp b & \text{if } \mu = \pm 1 \end{cases}, \quad (2.31)$$

where

$$c_0 = \frac{2}{5}, \quad c_{\pm 1} = -\frac{1}{5}. \quad (2.32)$$

For far-field E1 collisions, we use the expression $\bar{V}_{1\mu}^{\text{far}}(\mathbf{r}, \mathbf{R}) = V_{\text{E}1\mu}^{\text{rel}*}(b, z, \hat{\boldsymbol{\xi}} = \hat{\mathbf{r}})$ in Eq. (2.9) with $e_{\text{E}1}$ replaced by e .

We estimate the importance of close- and far-field collisions by using first-order time-dependent theory; we consider the contribution of one proton in P to the breakup process. The transition amplitudes due to the E1 field, from the initial state $\Phi_0(\boldsymbol{\xi})$ to the final one $\Phi_{c_f}(\boldsymbol{\xi})$, are given by

$$a_{1\mu}(b) = a_{1\mu}^{\text{close}}(b) + a_{1\mu}^{\text{far}}(b),$$

$$a_{1\mu}^{\text{close}}(b) = \frac{1}{i\hbar} \int_{-\infty}^{\infty} e^{i\omega t} \left\langle \Phi_{c_f}(\boldsymbol{\xi}) \left| \bar{V}_{1\mu}^{\text{close}}(\mathbf{r}, \mathbf{R}) \right| \Phi_0(\boldsymbol{\xi}) \right\rangle_{r>R} dt, \quad (2.33)$$

$$a_{1\mu}^{\text{far}}(b) = \frac{1}{i\hbar} \int_{-\infty}^{\infty} e^{i\omega t} \left\langle \Phi_{c_f}(\boldsymbol{\xi}) \left| \bar{V}_{1\mu}^{\text{far}}(\mathbf{r}, \mathbf{R}) \right| \Phi_0(\boldsymbol{\xi}) \right\rangle_{r<R} dt, \quad (2.34)$$

where ω represents the energy transfer as $\hbar\omega \equiv E_{c_f} - E_0$. Since we assume that the projectile moves along the z -axis with a constant velocity v , we immediately find $t = z/v$ and

$$\omega t = \frac{E_{c_f} - E_0}{\hbar c} \frac{z}{\beta}. \quad (2.35)$$

Using Eqs. (2.31)–(2.35), we obtain the explicit form of $a_{1\mu}^{\text{close}}$ and $a_{1\mu}^{\text{far}}$:

$$a_{1\mu}^{\text{close}}(b) = \frac{1}{i\hbar v} \sqrt{\frac{2\pi}{3}} Z_{\text{T}} e^2 \{g_0(\beta) + c_{\mu} g_2(\beta)\} \\ \times \int_{-\infty}^{\infty} dz \exp\left(i \frac{E_{c_f} - E_0}{\hbar c} \frac{z}{\beta}\right) \mathcal{M}_{1\mu}^{\text{close}}(R) \begin{cases} \sqrt{2}z & \text{if } \mu = 0 \\ \mp b & \text{if } \mu = \pm 1 \end{cases},$$

$$a_{1\mu}^{\text{far}}(b) = \frac{1}{i\hbar v} \sqrt{\frac{2\pi}{3}} \gamma Z_{\text{T}} e^2 \\ \times \int_{-\infty}^{\infty} dz \exp\left(i \frac{E_{c_f} - E_0}{\hbar c} \frac{z}{\beta}\right) \frac{\mathcal{M}_{1\mu}^{\text{far}}(R)}{(b^2 + \gamma^2 z^2)^{3/2}} \begin{cases} \sqrt{2}z & \text{if } \mu = 0 \\ \mp b & \text{if } \mu = \pm 1 \end{cases},$$

where

$$\mathcal{M}_{1\mu}^{\text{close}}(R) \equiv \left\langle \Phi_{c_f}(\boldsymbol{\xi}) \left| \frac{1}{r^2} Y_{1\mu}^*(\hat{\mathbf{r}}) \right| \Phi_0(\boldsymbol{\xi}) \right\rangle_{r>R}, \quad (2.36)$$

$$\mathcal{M}_{1\mu}^{\text{far}}(R) \equiv \left\langle \Phi_{c_f}(\boldsymbol{\xi}) \left| r Y_{1\mu}^*(\hat{\mathbf{r}}) \right| \Phi_0(\boldsymbol{\xi}) \right\rangle_{r<R}. \quad (2.37)$$

By comparing $a_{1\mu}(b)$ with $a_{1\mu}^{\text{far}}(b)$, we can evaluate how large far-field collisions contribute to the total breakup amplitude.

As a typical reaction, let us consider the Coulomb breakup of ${}^8\text{B}$. The ground state wave function reads

$$\Phi_0(\boldsymbol{\xi}) = u_0(\xi) Y_{1m_0}(\hat{\boldsymbol{\xi}}). \quad (2.38)$$

For the final state of ${}^8\text{B}$ after the breakup we choose a discretized continuum state with $l = 0$, i.e.,

$$\Phi_{c_f}(\boldsymbol{\xi}) = u_{c_f}(\xi) Y_{00}(\hat{\boldsymbol{\xi}}). \quad (2.39)$$

Here, $u_c(\xi)$ ($c = 0$ or c_f) is the radial part of $\Phi_c(\boldsymbol{\xi})$. Using Eqs. (2.38) and (2.39) together with $\mathbf{r} = (7/8)\boldsymbol{\xi}$, we have

$$\mathcal{M}_{1\mu}^{\text{close}}(R) = \frac{1}{\sqrt{4\pi}} \left(\frac{8}{7}\right)^2 \delta_{\mu, m_0} \int_{8R/7}^{\infty} u_{c_f}(\xi) u_0(\xi) d\xi, \quad (2.40)$$

$$\mathcal{M}_{1\mu}^{\text{far}}(R) = \frac{1}{\sqrt{4\pi}} \frac{7}{8} \delta_{\mu, m_0} \int_0^{8R/7} u_{c_f}(\xi) u_0(\xi) \xi^3 d\xi. \quad (2.41)$$

§3. Results and discussions

3.1. Numerical input

We use the same set of inputs as in Ref. 1) for the CDCC calculation of ${}^8\text{B}$ and ${}^{11}\text{Be}$ breakup reactions with ${}^{208}\text{Pb}$ target at 250 MeV/nucleon. The internal Hamiltonian of ${}^8\text{B}$ and ${}^{11}\text{Be}$ are the same as in Ref. 9) except that we neglect the spin of the proton and therefore we change accordingly the depth of the p - ${}^7\text{Be}$ potential to reproduce the proton separation energy of 137 keV. Note that in Ref. 9), and also in this work, the spins of neutron and C are disregarded. We account for s, p, d, and f-states in p - ${}^7\text{Be}$ and n - ${}^{11}\text{Be}$. The maximum value of the relative wave number, k_{max} , is 0.66 fm^{-1} for all such states. The number of discretized continuum states is 20 and 10 for the s-waves and the other waves, respectively, for both ${}^8\text{B}$ and ${}^{11}\text{Be}$. The optical potentials for the constituents of P, i.e., p , n , ${}^7\text{Be}$, and ${}^{11}\text{Be}$, on ${}^{208}\text{Pb}$ are the same as in Table I of Ref. 9). The maximum value used for the internal coordinate ξ is 200 fm, and the maximum impact parameter is 400 fm for both ${}^8\text{B}$ and ${}^{11}\text{Be}$ breakup reactions.

Note that in the present work, a *relativistic* calculation means a calculation which includes dynamical relativistic corrections in the nuclear and Coulomb coupling potentials. Also, a relativistic treatment of the kinematics is adopted in all the calculations shown below. Furthermore, we add quantum mechanical (QM) corrections in the breakup amplitudes obtained with the relativistic E-CDCC as described in §2.1; we use the results of fully QM but nonrelativistic CDCC for the amplitudes corresponding to $b \leq 18 \text{ fm}$ for both reactions. This prescription has been numerically tested and the results are shown in §3.4. We assume, as in Ref. 1), the far-field approximation to obtain the relativistic form of the Coulomb interaction between each constituent of the projectile and the target nucleus. The validity of this assumption is evaluated in §3.5.

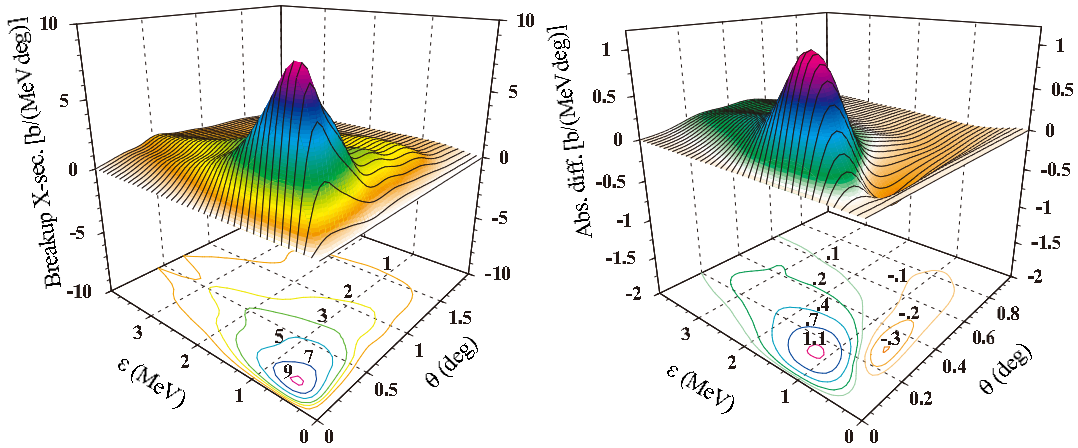


Fig. 1. Double differential breakup cross section (DDBUX) for ${}^8\text{B}+{}^{208}\text{Pb}$ at 250 MeV/nucleon including dynamical relativistic corrections (left panel), and its difference from the calculation without relativistic corrections (right panel).

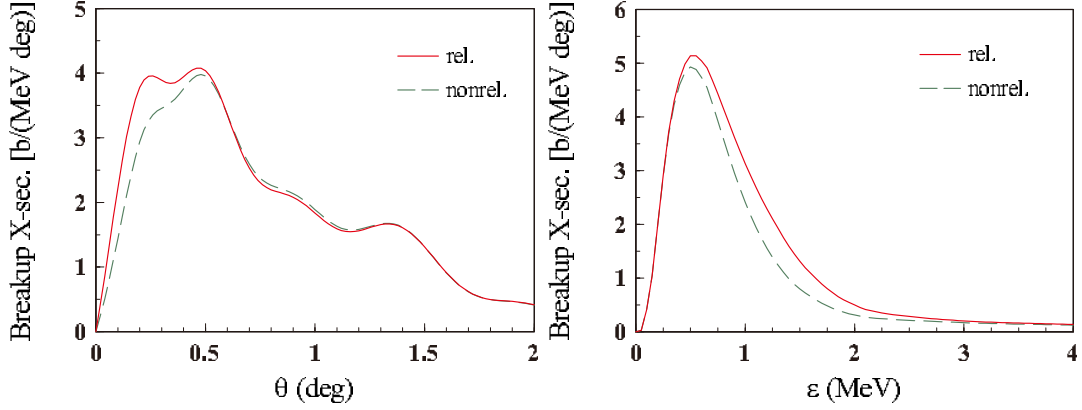


Fig. 2. Comparison between DDBUX, for the ${}^8\text{B}+{}^{208}\text{Pb}$ reaction at 250 MeV/nucleon, obtained with relativistic (solid line) and nonrelativistic (dashed line) calculations. The left panel shows the DDBUX with $\epsilon = 1.5$ MeV as a function of θ , while the right panel displays the DDX with $\theta = 0.06^\circ$ as a function of ϵ .

3.2. Dynamical relativistic effects on breakup cross section

In the left panel of Fig. 1 we show the double differential breakup cross section (DDBUX), $d^2\sigma_{\text{BU}}/(d\epsilon d\theta)$, for the ${}^8\text{B}+{}^{208}\text{Pb}$ reaction at 250 MeV/nucleon calculated with relativistic CDCC based on Eq. (2-21). ϵ is the relative energy of the two fragments of the projectile after the breakup, and θ is the scattering angle of the c.m. of the projectile. The right panel displays the difference of the DDBUX shown in the left panel from that calculated with nonrelativistic CDCC, which also is based on Eq. (2-21) but including no dynamical relativistic corrections. One observes a rather large increase in the DDBUX due to relativity at forward angles ($\theta \lesssim 0.2^\circ$) and around $\epsilon = 1$ MeV, where the DDBUX has quite large values as shown in the left panel. To show this effect more clearly, we plot the DDBUX with ϵ (θ) fixed at 1.5 MeV (0.06°) in the left (right) panel of Fig. 2. The results of the

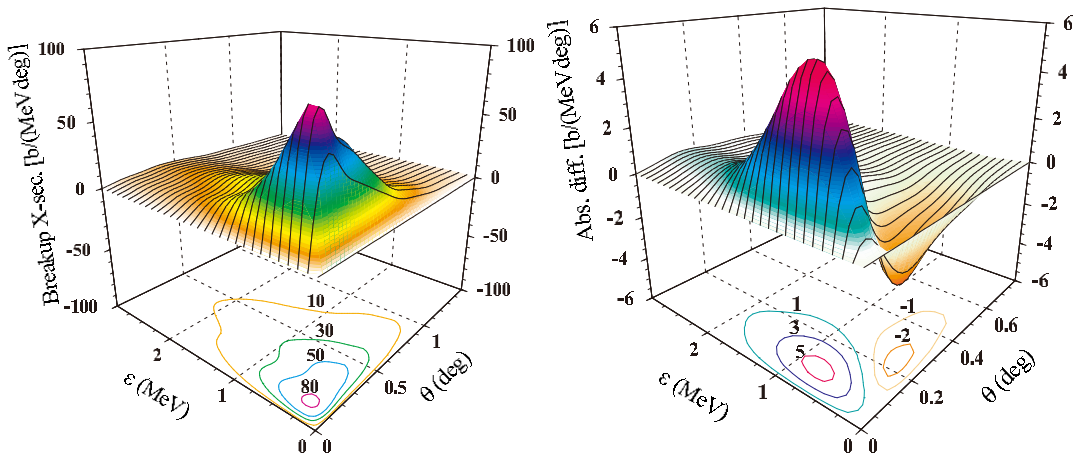


Fig. 3. Same as in Fig. 1 but for ${}^{11}\text{Be}+{}^{208}\text{Pb}$ at 250 MeV/nucleon.

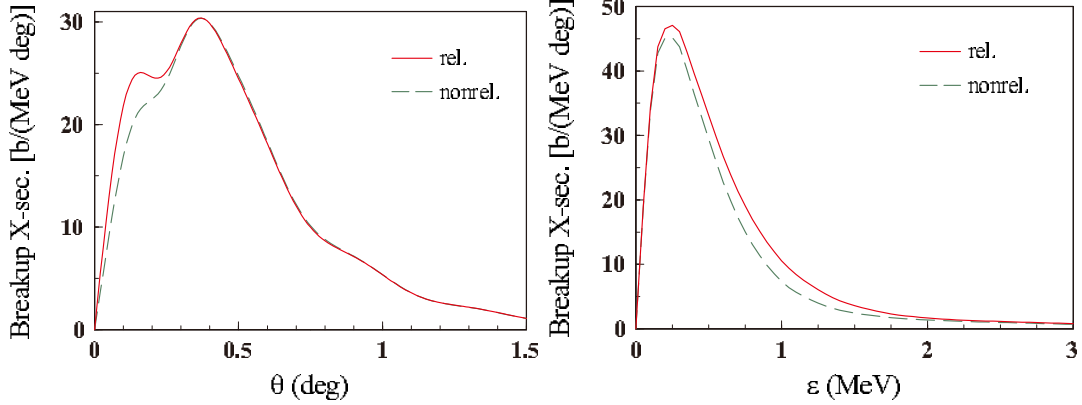


Fig. 4. Same as in Fig. 2 but for $^{11}\text{Be}+^{208}\text{Pb}$ at 250 MeV/nucleon; the left (right) panel corresponds to the DDBUX with $\epsilon = 1.0$ MeV ($\theta = 0.04^\circ$) as a function of θ (ϵ).

relativistic and nonrelativistic CDCC calculation are shown by the solid and dashed lines, respectively.

The results for the $^{11}\text{Be}+^{208}\text{Pb}$ reaction at 250 MeV/nucleon are shown in Figs. 3 and 4, in the same way as in Figs. 1 and 2, respectively. Features of the results are very similar to those of the $^8\text{B}+^{208}\text{Pb}$ reaction, except that 1) the magnitude of the DDBUX is much larger than that of ^8B and 2) the increase in the DDBUX due to relativity is slightly smaller and limited at smaller angles. The larger magnitude of the DDBUX arises from the larger value of the E1 effective charge e_{E1} of ^{11}Be compared with that of ^8B . The smaller effect of relativity for this reaction can be understood by the decomposition of the breakup cross section (BUX) into the components corresponding to individual partial waves of the projectile.

In the left (right) panel of Fig. 5 we show the BUX to the s-, p-, d-, and f-

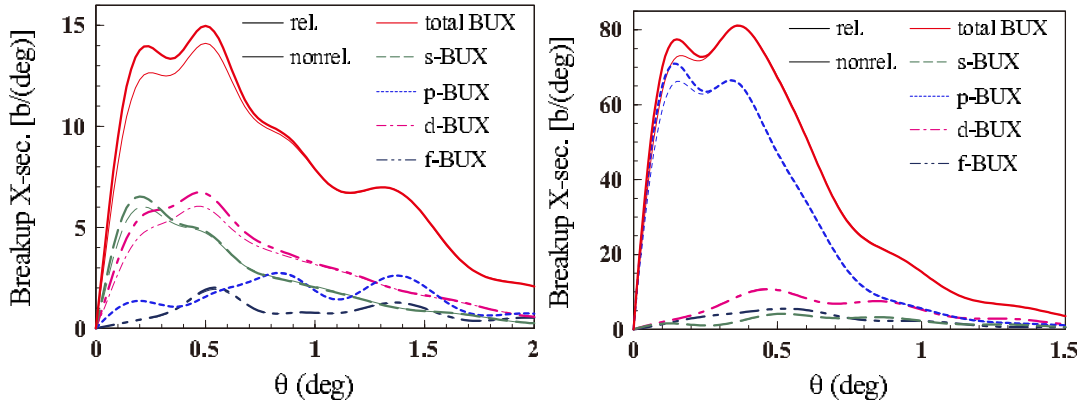


Fig. 5. Angular distribution of the breakup cross sections (BUX) to the s-, p-, d-, and f-states of the projectile are shown by the dashed, dotted, dash-dotted, and dash-dot-dotted lines, respectively, and the solid line represents the sum of them. The thick (thin) lines are the results of the relativistic (nonrelativistic) calculation. The left and right panels correspond to the $^8\text{B}+^{208}\text{Pb}$ and $^{11}\text{Be}+^{208}\text{Pb}$ reactions, respectively.

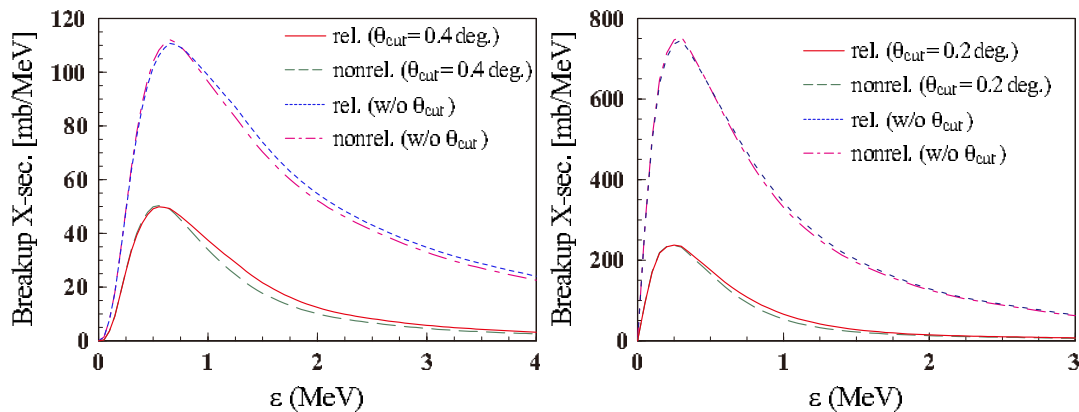


Fig. 6. Breakup energy spectra for ${}^8\text{B}+{}^{208}\text{Pb}$ at 250 MeV/nucleon (left panel). The solid and dashed lines show the results of the relativistic and nonrelativistic calculations, respectively, with a maximum c.m. scattering angle, θ_{max} , equal to 0.4° . The dotted (dash-dotted) line is the same as the solid (dashed) line but $\theta_{\text{max}} = 5.0^\circ$. Results for ${}^{11}\text{Be}+{}^{208}\text{Pb}$ at 250 MeV/nucleon are shown in the right panel. Here, $\theta_{\text{max}} = 0.2^\circ$ (3.0°) for the solid and dashed (dotted and dash-dotted) lines.

waves of ${}^8\text{B}$ (${}^{11}\text{Be}$) by the dashed, dotted, dash-dotted, and dash-dot-dotted lines, respectively; the solid line is the sum of them. Note that the cross sections are obtained by integrating the DDBUX over ϵ . In each panel, the thick and thin lines represent the results of relativistic and nonrelativistic CDCC, respectively. Since the ground state of ${}^8\text{B}$ is the p-wave, s- and d-state BUX are dominant in the breakup of ${}^8\text{B}$, as the E1 transition gives the dominant contribution to the breakup reactions caused by a heavy target nucleus. For the breakup of ${}^{11}\text{Be}$, the ground state of which is assumed here to be an s-wave, the dominant contribution is to the p-wave. One finds the increase of BUX due to relativity only in the p-wave channel, corresponding to the E1 transitions. The increase (due to relativity) in the s-wave BUX of ${}^8\text{B}$ has the same feature as that of the p-wave BUX of ${}^{11}\text{Be}$. For the ${}^8\text{B}$ breakup, the increase in the d-wave BUX is also noticeable, which makes the relativistic effects on the total BUX of ${}^8\text{B}$ more significant.

In the analysis of a breakup experiment using a heavy target, a cutoff value for θ , θ_{cut} , is usually introduced which aims to eliminate contributions from nuclear-induced breakup. Since the increase in the DDBUX due to relativity is located at forward angles, such an analysis with θ_{cut} requires a relativistic description of the breakup reaction. This is clearly shown in Fig. 6, where the θ_{cut} dependence of the relativistic effects on the breakup energy spectrum is plotted. The left and right panels correspond to the ${}^8\text{B}$ and ${}^{11}\text{Be}$ breakup reactions, respectively. The solid (dotted) and dashed (dash-dotted) lines represent the results of relativistic and nonrelativistic CDCC with (without) θ_{cut} , respectively. Here, $\theta_{\text{cut}} = 0.4^\circ$ (0.2°) is used for the ${}^8\text{B}$ (${}^{11}\text{Be}$) breakup. One sees that the use of a cutoff angle θ_{cut} enhances the relativistic effects. Note that preceding analyses of Coulomb breakup processes using the virtual photon method, or first-order perturbation theory, included relativistic effects properly. They would give, however, very different results from those of rel-

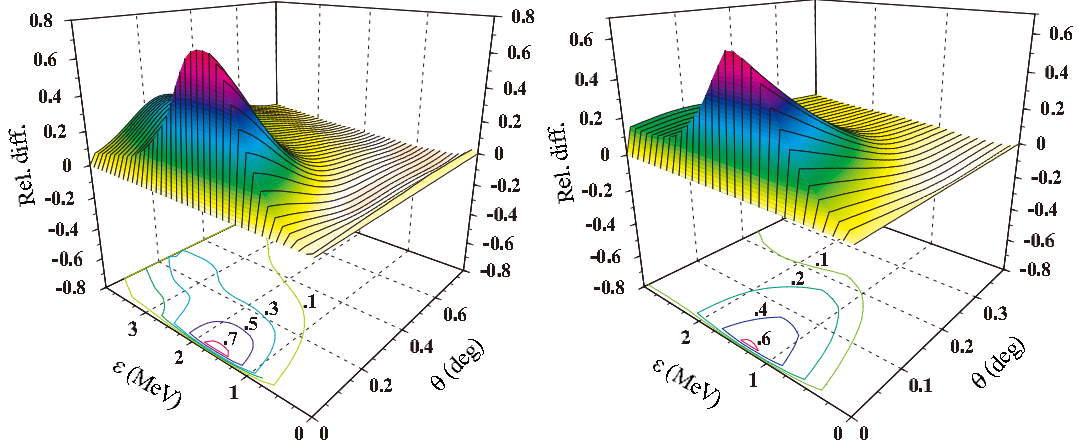


Fig. 7. Relative difference of the relativistic DDX from the nonrelativistic one. The left and right panels respectively correspond to ${}^8\text{B}+{}^{208}\text{Pb}$ and ${}^{11}\text{Be}+{}^{208}\text{Pb}$ at 250 MeV/nucleon.

ativistic CDCC, because of the contributions of nuclear breakup and higher-order processes in Coulomb breakup, as shown in §3.3.

Our conclusions based on the previous figures are better seen if we plot relative differences of the several effects we want to discuss here. For example, we show in the left (right) panel of Fig. 7 the relative difference of the DDBUX obtained with relativistic CDCC from that with nonrelativistic CDCC, for the ${}^8\text{B}$ (${}^{11}\text{Be}$) breakup. The difference is indeed large (several tens of % level), which shows the importance of the relativistic effects on the DDBUX.

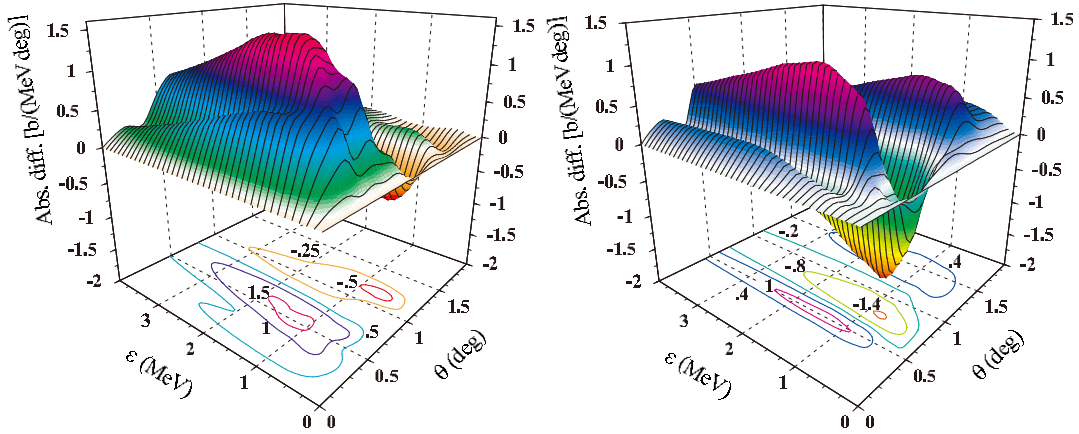


Fig. 8. The left panel shows the difference of the DDBUX for ${}^8\text{B}+{}^{208}\text{Pb}$ at 250 MeV/nucleon obtained with a first-order calculation from that obtained with CDCC. The right panel shows the difference of the DDX obtained with CDCC including nuclear and Coulomb breakup to that with only Coulomb breakup. In all calculations we take into account dynamical relativistic corrections.

3.3. Higher-order effects and nuclear breakup

As shown in Ref. 1), the contribution of nuclear breakup as well as higher-order effects on the BUX is very important, even at 250 MeV/nucleon. We show in the left panel of Fig. 8 the absolute difference of the DDBUX for ${}^8\text{B}+{}^{208}\text{Pb}$ calculated with first order perturbation theory from that with relativistic CDCC, which we call here *higher-order corrections*. The right panel shows the difference of the DDBUX obtained with relativistic CDCC, which includes both nuclear and Coulomb breakup, from that including only the Coulomb breakup. We call this difference *nuclear breakup correction*; the effects of the interference between the nuclear and Coulomb breakup amplitudes are also included. One sees the higher-order and nuclear breakup corrections are of the order of 10%. They have a rather weak ϵ dependence, while they oscillate with respect to θ .

As shown in the left panel of Fig. 5, all partial-wave components of the BUX of ${}^8\text{B}$ are comparable at $\theta \gtrsim 0.5^\circ$. This feature results in a non-trivial change in each BUX component due to the inclusion of higher-order processes or nuclear breakup. On the other hand, these corrections for ${}^{11}\text{Be}$ breakup, as shown in Fig. 9, display a simpler distribution on the ϵ - θ plane. We find from a detailed analysis that since the p-state BUX is dominant for the ${}^{11}\text{Be}$ breakup, the change in the p-state BUX due to the inclusion of the higher-order processes or nuclear breakup and that in other small BUX components add up almost incoherently.

3.4. Quantum mechanical effects

An important feature of the present CDCC calculation is that the quantum mechanical (QM) correction is explicitly included. This is possible because, as discussed in Ref. 1), relativistic corrections in the continuum-continuum couplings are only appreciable for the breakup amplitudes corresponding to large values of L , i.e., for large orbital angular momenta of relative motion between the projectile and target, where the QM correction is negligibly small.^{3),4)} Note that inclusion of the relativistic Coulomb and nuclear coupling potentials in a QM calculation, based on

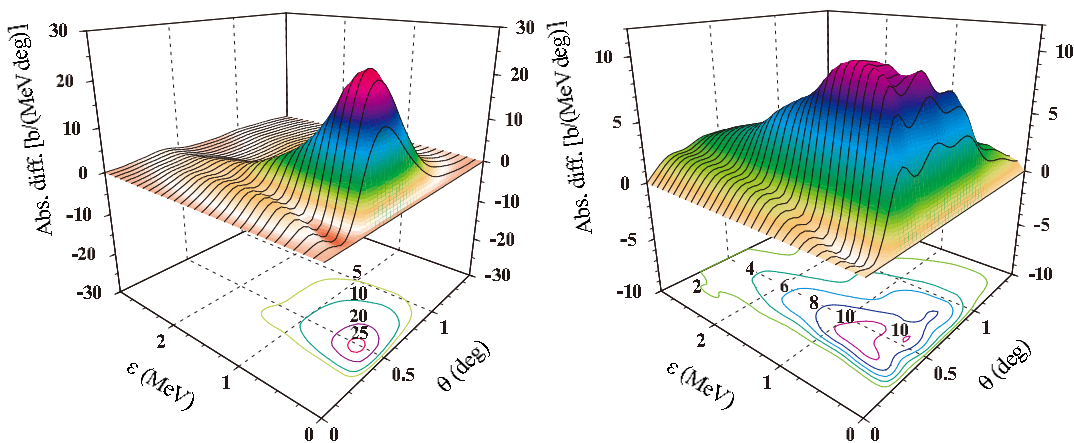


Fig. 9. Same as in Fig. 7 but for ${}^{11}\text{Be}+{}^{208}\text{Pb}$ at 250 MeV/nucleon.

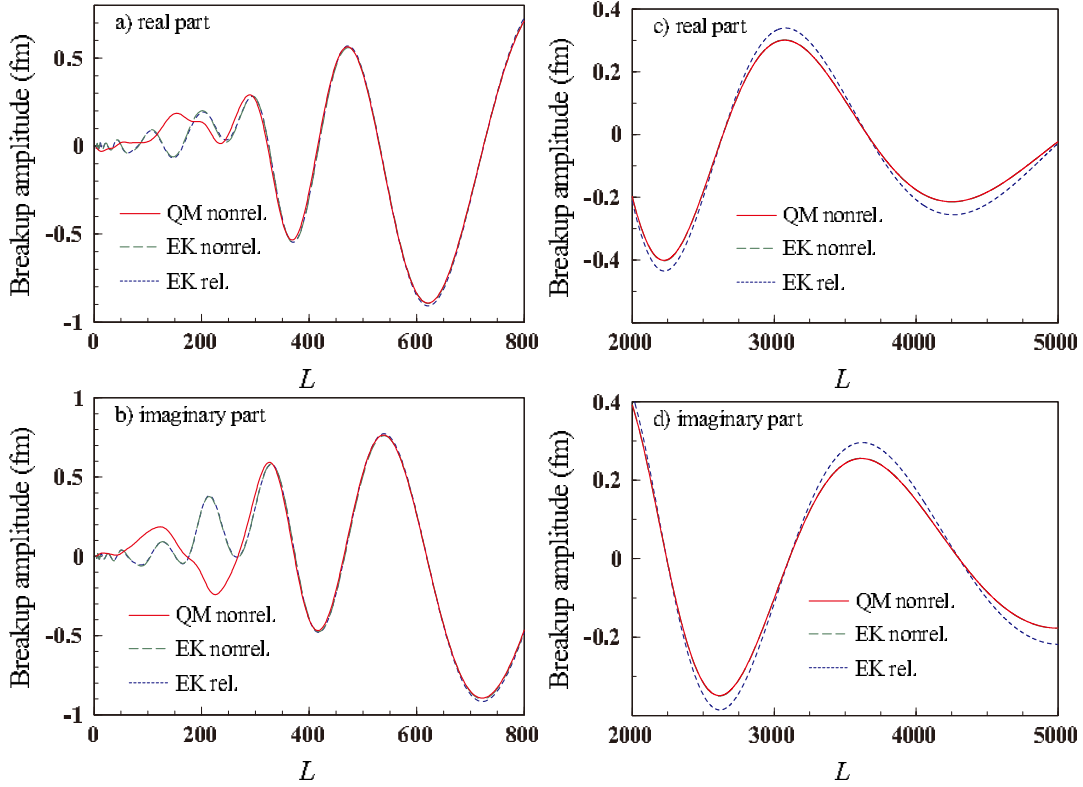


Fig. 10. Breakup amplitude for ${}^8\text{B}+{}^{208}\text{Pb}$ at 250 MeV/nucleon as a function of the orbital angular momentum L between ${}^8\text{B}$ and ${}^{208}\text{Pb}$. The final state of ${}^8\text{B}$ is chosen to be the s-wave 6th bin state, and the z -component m_0 of the spin of ${}^8\text{B}$ in the incident channel chosen as 1. The solid, dashed, and dotted lines show the results of nonrelativistic quantum mechanical CDCC, nonrelativistic eikonal CDCC, and relativistic eikonal CDCC, respectively. The upper (lower) panels correspond to the real and imaginary parts of the breakup amplitude.

a conventional partial wave decomposition, is very complicated.

We show in Fig. 10 the breakup amplitudes for ${}^8\text{B}+{}^{208}\text{Pb}$ at 250 MeV/nucleon as a function of L . We choose the s-wave 6th bin state, whose breakup amplitude has the largest value, as a final state; the z -component m_0 of the spin of ${}^8\text{B}$ in the incident channel is chosen as 1. The upper and lower panels correspond to the real and imaginary parts of the amplitude, respectively. The solid line represents the result of nonrelativistic QM CDCC, which adopts Eq. (2·20) for all L and has no dynamical relativistic corrections. The dotted and dashed lines are the results of E-CDCC, based on Eq. (2·17), with and without dynamical relativistic corrections; below we call the former relativistic E-CDCC and the latter nonrelativistic E-CDCC. One sees from the figure that at small L , i.e., $L \lesssim 500$, the dashed and dotted lines agree very well with each other, and deviate from the solid line. On the other hand, at large L , the solid and dashed lines show a very good agreement and differ from the dotted line. This is indeed consistent with the above mentioned properties of relativistic and QM corrections with respect to L . Thus, using the amplitude obtained by nonrelativistic

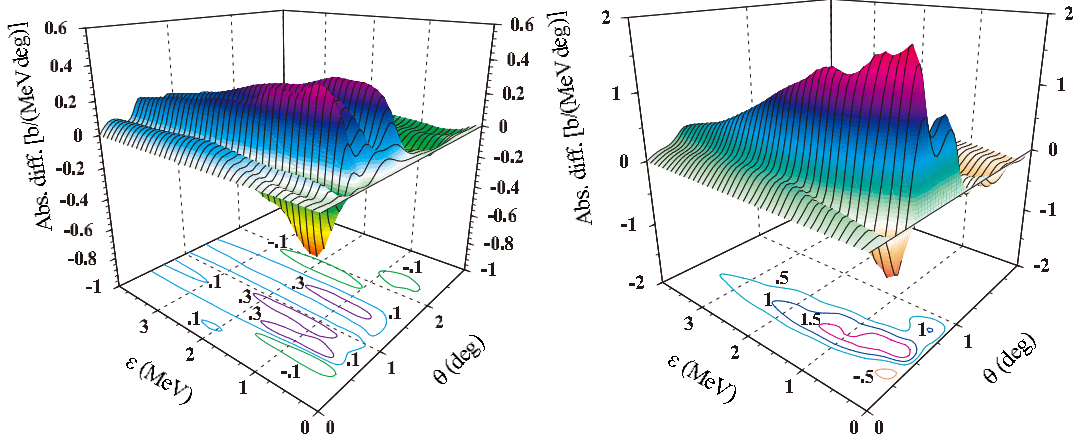


Fig. 11. Difference of the DDX obtained with nonrelativistic quantum-mechanical CDCC from that obtained with nonrelativistic eikonal CDCC. The left (right) panel corresponds to ${}^8\text{B}+{}^{208}\text{Pb}$ (${}^{11}\text{Be}+{}^{208}\text{Pb}$) at 250 MeV/nucleon.

QM CDCC for small L and those by relativistic E-CDCC for large L allows one to construct an accurate CC framework that includes dynamical relativistic corrections and QM effects, i.e., relativistic CDCC adopted in §3.2 and 3.3.

The difference of the DDBUX with nonrelativistic QM CDCC from that with nonrelativistic E-CDCC is shown in Fig. 11. The left and right panels correspond to ${}^8\text{B}+{}^{208}\text{Pb}$ and ${}^{11}\text{Be}+{}^{208}\text{Pb}$ at 250 MeV/nucleon, respectively. Compared to the higher-order and nuclear breakup corrections, the difference due to the QM effect, i.e., the *QM correction*, seems very small. It is appreciable, however, in the angular distribution of the BUX, as shown in Fig. 12. The solid and dashed lines represent the BUX obtained with nonrelativistic QM CDCC and nonrelativistic E-CDCC, respectively. For both ${}^8\text{B}+{}^{208}\text{Pb}$ (left panel) and ${}^{11}\text{Be}+{}^{208}\text{Pb}$ (right panel) reactions,

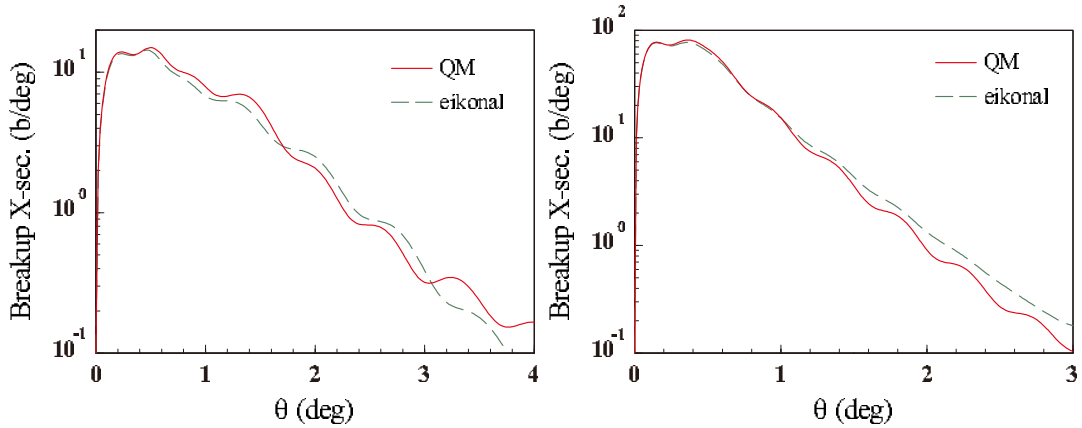


Fig. 12. Breakup cross sections for ${}^8\text{B}+{}^{208}\text{Pb}$ (left panel) and ${}^{11}\text{Be}+{}^{208}\text{Pb}$ (right panel) at 250 MeV/nucleon as a function of the scattering angle. The solid and dashed lines show the results of nonrelativistic quantum mechanical CDCC and nonrelativistic eikonal CDCC, respectively.

the θ dependence of the BUX at angles above the peak position is indeed sensitive to the QM correction.

3.5. Role of close-field collisions

Finally, we evaluate the validity of the far-field approximation for the Coulomb interaction used in this study. Figure 13 shows the breakup amplitude multiplied by a weight value b . The left and right panels show the results for $m_0 = \mu = 0$ and 1, respectively, obtained with the first order perturbation model described in §2.2. In each panel, the solid (dashed) line shows the amplitude corresponding to both the close and far fields (only the far field). It is clearly seen that the contribution from the close field of the Coulomb interaction is negligibly small. We expect that the inclusion of higher order processes and the nuclear breakup does not change this conclusion.

In Ref. 10) the close-field contribution is shown to be important at lower energies, i.e., $E \lesssim 50$ MeV/nucleon. At these low energies, however, the dynamical relativistic effects are very small and we do not need the far-field approximation that is used only to obtain the transformation form of the Coulomb coupling potentials due to relativity. Note that in the evaluation of the nonrelativistic Coulomb potentials, Eq. (2.6), both close and far fields are taken into account.

§4. Summary

The dynamical relativistic effects on the ${}^8\text{B}$ and ${}^{11}\text{Be}$ double differential breakup cross sections (DDBUX) at 250 MeV/nucleon are investigated in detail by means of the Continuum-Discretized Coupled-Channels method (CDCC). The effects on the DDBUX are indeed large, i.e., several tens of % at forward angles θ and at slightly higher breakup energies ϵ than at the peak of the breakup energy spectrum. The contribution of the nuclear breakup and higher-order processes are found to be the order

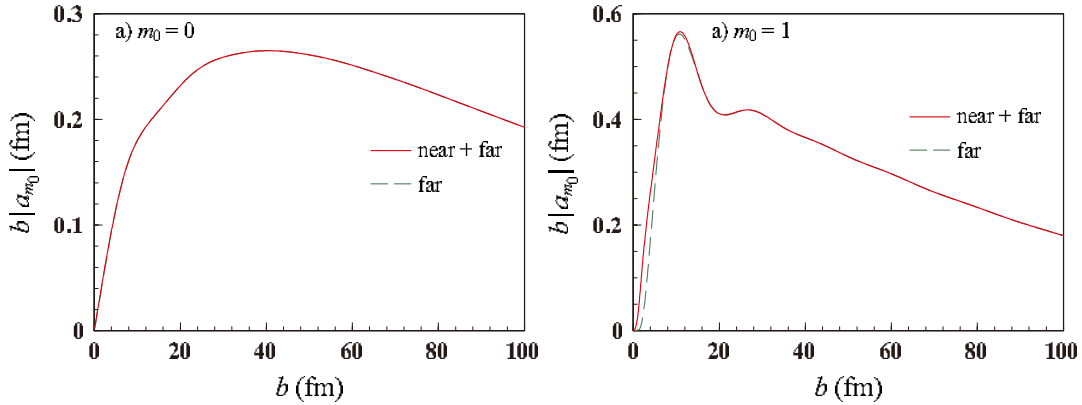


Fig. 13. Weighted breakup amplitude for ${}^8\text{B}+{}^{208}\text{Pb}$ at 250 MeV/nucleon as a function of the impact parameter b . The final state of ${}^8\text{B}$ is the same as in Fig. 5. The left and right panels correspond to $m_0 = \mu = 0$ and 1, respectively. In each panel, the solid (dashed) line shows the result including both far and close contributions (only the far contribution).

of 10% and has different θ - ϵ dependence between the ^8B and ^{11}Be breakup processes. It is confirmed that the relativistic corrections are only appreciable for breakup amplitudes corresponding to large impact parameters, and quantum-mechanical correction is negligible there. This feature enables one to perform fully relativistic and quantum mechanical coupled-channel calculations of breakup reactions at intermediate energies. The far-field approximation, which is used in the formulation of relativistic Coulomb coupling potentials, is justified numerically by means of a first-order perturbative calculation. Thus, we now have an accurate method to analyze experimental data of nuclear and Coulomb breakup reactions at intermediate energies by means of *relativistic CDCC*. Inclusion of magnetic transitions will be an important future work.

Acknowledgements

This work was partially supported by the U.S. DOE grants DE-FG02-08ER41533 and DE-FC02-07ER41457 (UNEDF, SciDAC-2), the Research Corporation, and the JUSTIPEN/DOE Grant DEFG02-06ER41407. The computation was carried out using the computer facilities at the Research Institute for Information Technology, Kyushu University.

References

- 1) K. Ogata and C. A. Bertulani, Prog. Theor. Phys. **121** (2009), 1399.
- 2) M. Kamimura, M. Yahiro, Y. Iseri, Y. Sakuragi, H. Kameyama, and M. Kawai, Prog. Theor. Phys. Suppl. No. 89 (1986), 1.
N. Austern, Y. Iseri, M. Kamimura, M. Kawai, G. Rawitscher and M. Yahiro, Phys. Rep. **154** (1987), 125
- 3) K. Ogata, M. Yahiro, Y. Iseri, T. Matsumoto and M. Kamimura, Phys. Rev. C **68** (2003), 064609.
- 4) K. Ogata, S. Hashimoto, Y. Iseri, M. Kamimura and M. Yahiro, Phys. Rev. C **73** (2006), 024605.
- 5) C. A. Bertulani, Phys. Rev. Lett. **94** (2005), 072701.
- 6) H. Feshbach and M. Zabeck, Ann. of Phys. **107** (1977) 110.
- 7) H. Esbensen and C. A. Bertulani, Phys. Rev. C **65** (2002), 024605.
- 8) C. A. Bertulani, C. M. Campbell, and T. Glasmacher, Comp. Phys. Comm. **152** (2003) 317.
- 9) M. S. Hussein, R. Lichtenthaler, F. M. Nunes and I. J. Thompson, Phys. Lett. B **640** (2006), 91.
- 10) H. Esbensen and G. F. Bertsch, Phys. Rev. C **66** (2002), 044609.